



The microscopic distribution of hydrophilic polymers in interpenetrating polymer networks (IPNs) of medical grade silicone

Gregory N. Smith^{a,b,*}, Erik Brok^b, Martin Schmiele^b, Kell Mortensen^b, Wim G. Bouwman^c, Chris P. Duif^c, Tue Hassenkam^d, Martin Alm^e, Peter Thomsen^e, Lise Arleth^b

^a ISIS Neutron and Muon Source, Science and Technology Facilities Council, Rutherford Appleton Laboratory, Didcot, OX11 0QX, United Kingdom

^b Niels Bohr Institute, University of Copenhagen, Universitetsparken 5, 2100 Copenhagen Ø, Denmark

^c Faculty of Applied Sciences, Delft University of Technology, 2629, JB Delft, the Netherlands

^d Department of Chemistry, University of Copenhagen, Universitetsparken 5, 2100 Copenhagen Ø, Denmark

^e BioModics ApS, 2610 Rødovre, Denmark

ARTICLE INFO

Keywords:

Interpenetrating polymer network
Neutron scattering
Atomic force microscopy

ABSTRACT

By introducing hydrophilic polymers into silicone medical devices, highly beneficial biomedical properties can be realized. An established solution to introduce hydrophilic polymers is to form an interpenetrating polymer network (IPN) by performing the hydrogel synthesis in the presence of silicone swollen in supercritical carbon dioxide. The precise distribution of the two polymers is not known, and determining this is the goal of this study. Neutron scattering and microscopy were used to determine the distribution of the hydrophilic guest polymer. Atomic force microscopy revealed that the important length scale on the surface of these materials is 10–100 nm, and spin-echo small-angle neutron scattering (SESANS) on IPNs submerged in D₂O revealed structures of the same scale within the interior and enabled quantification of their size. SESANS with hydration by D₂O proved to be the only scattering technique that could determine the structure of the bulk of these types of materials, and it should be used as an important tool for characterizing polymer medical devices.

1. Introduction

Many medical devices are made of silicone elastomers due to their advantageous properties: soft and flexible, yet tough and robust, highly chemically resistant, and with good biocompatibility. The hydrophobic surface of silicones makes them prone to bacterial attachment, which can lead to biofilm formation and hospital acquired infections [1]. Due to the high surface tension of water [2], it is energetically favorable for cells to attach to surfaces rather than remain in the medium, and making the surface of medical devices more hydrophilic can alleviate this. Hydrophilic surfaces could be created in several ways. Biomaterials could be produced solely from hydrogels, but these have poor mechanical properties [3,4]. Hydrophilic coatings could be applied, but they are difficult to maintain. Interpenetrating polymer networks (IPNs), networks of interlaced materials on a molecular scale that are not covalently bonded and cannot be separated unless chemical bonds are broken [5], are another way to increase the surface tension of medical devices [4]. These are the type of materials that will be studied here.

Two types of manufacturing techniques for producing IPNs exist: the simultaneous method (where the two networks are synthesized simultaneously via orthogonal paths) and the sequential method (where one network is synthesized within an already prepared one) [6]. We prepared IPNs using the sequential method from silicones and hydrogels where supercritical CO₂ was used to introduce the hydrophilic, hydrogel-forming monomers into the swollen silicone, as previously reported in the literature [7–12]. Supercritical CO₂ ($T_c = 31.1^\circ\text{C}$, $P_c = 73.8\text{ bar}$) is an attractive synthesis medium, due to its gas-like diffusion and liquid-like density, which can be tuned easily by changes in pressure [13]. Polydimethylsiloxane (PDMS), an example silicone, is known to have, for a non-fluorinated polymer, an extremely high solubility in supercritical CO₂, which makes cross-linked silicones swellable in the solvent [14].

Despite this previous work, the precise distribution of the two polymers is not yet well-understood. Are the two networks fully intertwined? Do they phase separate into hydrophilic and hydrophobic domains? Significant previous research effort has shown that these IPNs

* Corresponding author. ISIS Neutron and Muon Source, Science and Technology Facilities Council, Rutherford Appleton Laboratory, Didcot, OX11 0QX, United Kingdom.

E-mail address: gregory.smith@stfc.ac.uk (G.N. Smith).

<https://doi.org/10.1016/j.polymer.2021.123671>

Received 15 January 2021; Received in revised form 12 March 2021; Accepted 15 March 2021

Available online 22 March 2021

0032-3861/© 2021 The Author(s). Published by Elsevier Ltd. This is an open access article under the CC BY license (<http://creativecommons.org/licenses/by/4.0/>).

are known to act as efficient drug delivery systems [7–9,15,16], to treat or inhibit infections associated with catheters [17,18], and to release antibiotics and provide effective antimicrobial surfaces [7,8,11,12]. The efficacy of these beneficial properties will be controlled by the distribution of the two polymers (hydrophilic hydrogel and silicone), but previous efforts using microscopy have not been able to reveal this [7,10,19]. Therefore, finding a way of characterizing the structure of these IPNs is important.

As imaging techniques have so far prevented direct determination of the distribution of the hydrogel network, scattering techniques were used as the primary tools. Although there are several reports on investigating the structure of IPNs by small-angle scattering (SAS) [20–26], the number of reports on the structure of silicone-hydrogel IPNs is limited [21,25–27]. Data analysis on commercial silicones can be plagued by the presence of silica filler particles, which are introduced to improve the mechanical stability, but they can dominate the scattering. Despite the presence of fillers, devices made from medical grade silicones contain them, and to find methods that can study application-relevant systems requires accounting for their presence.

Neutron scattering, in particular, makes for an ideal method to study a material like this because it can highlight specific parts of the material, for example, by swelling the hydrogel with heavy water. The deuterium nuclei (^2H or D) in heavy water (D_2O) interact differently with neutrons than protium nuclei (^1H). When contrast is obtained in this way, the scattering from deuterated material should dominate over the scattering from the filler particles, and thus enable investigation of the hydrogel structure. A further advantage is that D_2O will only enter surface connected hydrogel, and it is thus exactly the hydrogel volume responsible for transporting polar small molecules (water or drugs) that will be highlighted. The differences in scattering length densities (SLDs), quantifying the molecular ability to scatter either X-rays or neutrons, between all the species used in this study are shown in Table 1. In Fig. 1, the contrasts for the different scattering techniques are shown schematically.

To achieve our goal of determining the distribution of the polymers in these IPNs, we use a combination of microscopy and scattering to study them. Atomic force microscopy (AFM) was used to image the surface of the IPNs. Neutron scattering (specifically the variant, spin-echo small-angle neutron scattering or SESANS) was used to study the morphology of the IPN. SESANS can access longer length scales (on order of $10\ \mu\text{m}$) than accessible by conventional SANS and in real space. Together these techniques enable a structural characterization of these IPNs in more detail than has previously been possible. As the potential of using these IPNs as medical devices has already been demonstrated by various assays [8–10], the focus is to study the distribution of the two polymers in the IPNs, which AFM and SESANS have been used to determine for the first time.

2. Experimental

2.1. Materials

Square SR330 MA/MB silicone is a medical grade material that was supplied by Shenzhen Square Silicone Materials Co., Ltd. (China). Sylgard 184 silicone was supplied by Dow Corning.

2-Hydroxyethyl methacrylate (HEMA, 97%) with 200 ppm monomethyl ether hydroquinone (MEHQ) as inhibitor, poly(ethylene glycol) methyl ether acrylate (PEGMEA, average $M_n = 480\ \text{g mol}^{-1}$) with 100 ppm butylated hydroxytoluene (BHT) and 100 ppm MEHQ as inhibitor, and ethylene glycol dimethacrylate (EGDMA) cross-linker were used as monomers for the hydrogel synthesis. An inhibitor remover column packed with quatamine divinylbenzene/styrene copolymer beads on Cl ion form (De-Hibit 200) supplied by Polysciences (USA) was used (following instructions given on the technical data sheet) to remove inhibitor before use. HEMA was further purified by distillation at reduced pressure, the fraction at $67\ ^\circ\text{C}$ and 3.5 mbar was collected. Both

Table 1

Mass densities (ρ_m) and X-ray (at $\text{Cu K}\alpha$) and neutron scattering length densities (ρ_X and ρ_N , respectively) of materials used. PHEMA and PDMS are used for the hydrogel and silicone components, respectively. (Note that the SLDs for PHEMA and PDMS are shown. The actual SLDs in this study may differ as the hydrogel is a copolymer of PHEMA, and the silicone is crosslinked elastomer.)

Compound	$\rho_m\ (\text{g cm}^{-3})$	$\rho_X\ (10^{-6}\ \text{\AA}^{-2})$	$\rho_N\ (10^{-6}\ \text{\AA}^{-2})$
PHEMA [28]	1.315	12.0	1.21
PDMS [29]	0.969	8.95	0.06
Silica (SiO_2) [30]	2.305	19.8	3.64
H_2O [31]	0.998	9.45	− 0.56
D_2O [32]	1.105	9.41	6.36

monomers were stored at $5\ ^\circ\text{C}$.

The cosolvents ethanol (EtOH, 99.9%) and tetrahydrofuran (THF) were all used as received. Oxygen-free CO_2 4.0 was supplied by Aga Denmark A/S (Denmark) and used as received.

All chemicals were supplied by Sigma–Aldrich (Germany), unless otherwise stated.

2.1.1. Host polymer

Two types of commercial silicone elastomer are used for the IPNs. Square SR330 MA/MB silicone was hot plate molded to hollow cylindrical specimens (length 4 cm, inner diameter 4.0 mm, wall thickness 0.5 mm). Sylgard 184 was mixed 20:1 then entrapped air was removed by applying a vacuum, the mixture was poured into Petri dish to make flat samples with a thickness of 2.0 mm. The silicone samples were then cured in an oven at $150\ ^\circ\text{C}$ for 18 h. We know from previous experience that the Square silicone contains nanoparticulate silica particles as mechanical fillers. These particles dominate the scattering of X-rays, and for this reason the samples based on Sylgard 184 silicone, which do not show the same amount of scattering from filler material, were also studied.

2.1.2. Initiator synthesis

Diethyl peroxydicarbonate (DEPDC) was synthesized according to literature [33,34] by reacting 12 ml ethyl chloroformate (122.5 mmol) with 6.64 ml 30% H_2O_2 (58.59 mmol) and 24 ml 5 M NaOH (120 mmol) in 100 ml pre-cooled demineralized water under stirring. The reactants were added drop-by-drop to ensure that the temperature never exceeded $10\ ^\circ\text{C}$. After gentle stirring for another 10 min, 50 ml of pre-cooled hexane was added, to extract DEPDC under increased stirring speed for 5 min. The mixture was transferred to a separation funnel and the organic phase was collected. The separation was repeated twice. The produced DEPDC was stored in hexane at $-18\ ^\circ\text{C}$. The concentration of DEPDC in hexane was measured by titration with iodine to 0.2 M according to ASTM method E298-17a. The initiator mixture is regularly examined by semi-quantitative peroxide test stick Quantofix method supplied by Macherey–Nagel (Germany).

2.1.3. Fabrication of IPNs

In a typical experiment a 0.5–1.0 g silicone specimen was placed on a metal grid in a 16 ml stainless steel high-pressure reactor equipped with a magnet for stirring. 0.60–1.60 ml HEMA, 1.60 ml PEGMEA, 0.096 ml EGDMA, 0.80 ml 0.20 M DEPDC in hexane, 1.12 ml EtOH and 1.12 ml THF were added and the mixture was stirred while heating the reactor to $40\ ^\circ\text{C}$. Then CO_2 was added through a P-50 high pressure pump from Thar (USA) to ensure a pressure of 300 bar at $40\ ^\circ\text{C}$. After 19 h the pressure was slowly released. The IPNs were then collected and washed gently in tap-water for removal of excess polymer. Excess monomer and non-cross-linked polymer were extracted by placing the IPN samples in 96 vol % EtOH for one week. The hydrogel content of the IPNs were determined gravimetrically.

The procedure resulted in the following sample series. The parameter xx denote the wt. % of hydrogel.

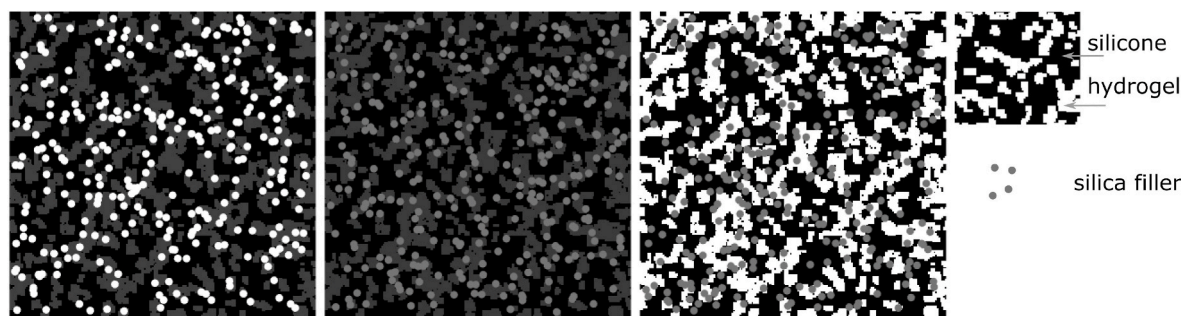


Fig. 1. Schematic of the contrast for hydrated-hydrogel in silicone for different scattering measurements. (Left) In an X-ray scattering measurement, the hydrogel is effectively matched to the silicone, and the structure of the silica filler is dominating. (Middle) For H₂O-hydrated hydrogel in a neutron scattering measurement, the hydrogel has a small contrast with the silicone but so does the silica filler. (Right) For D₂O-hydrated hydrogel in a neutron scattering measurement, the hydrogel has a very large contrast with the silicone, and the hydrogel structure dominates the scattering.

- Samples based on Square silicone: Sqr-xx series, xx = 00, 20, 26, 34, 42, 51
- Samples based on Sylgard 184 silicone: Syl-xx series, xx = 00, 12, 22, 32

For the different experiments, samples that were dry, samples that were soaked in deionized H₂O (Milli-Q), and samples that were soaked in 99.9 atom % D D₂O (purchased from Cambridge Isotope Laboratories) were prepared.

2.2. Water content

The equilibrium water content (EWC) of the IPNs was measured by measuring the masses m_{swelled} and m_{dry} of the samples before and after drying.

$$EWC = \frac{m_{\text{swelled}} - m_{\text{dry}}}{m_{\text{swelled}}} \quad (1)$$

Sqr-IPN samples were soaked in water for one week to ensure that the degree of swelling had reached equilibrium, by monitoring the sample mass. According to literature, 20 h should be sufficient to reach EWC of similar IPNs [7], but thickness and morphology affects the kinetics of water uptake.

The EWC determined for IPNs containing between 20% and 51% hydrogel are shown in Table 2. A monotonic relationship is found between the amount of hydrogel and EWC, indicating that all hydrogel in the IPNs is surface-connected and that swelling is not restricted by the silicone host polymer.

2.3. Atomic force microscopy (AFM)

AFM measurements were performed using an Asylum Research MFP-3DAFM with software from AtomicforceDE to generate the AFM images and force maps. The tip was an Olympus AC240, with nominal spring constant of 2 N m⁻¹ and a resonance frequency around 70 kHz. To generate the AFM images, an AC-mode with a scan rate of 1 Hz was used. To generate force maps, the maximum adhesion during a 1 μm pull after indenting the tip with a 10 nN trigger force with a scan rate of 4 Hz and

50 × 50 data points over an 1 × 1 μm² area was recorded. The force map was done using the same instrument and tip, now in deionized ultrapure water.

2.4. Scattering

Small-angle X-ray scattering (SAXS), small-angle neutron scattering (SANS), and spin-echo small-angle neutron scattering (SESANS) measurements were all performed. SAXS and SANS measurements were not able to provide conclusive information, and full details of these are only provided in the Supporting Information.

2.4.1. Small-angle X-ray scattering (SAXS)

SAXS experiments were performed with a lab-based micro-focus SWAXS camera (Ganesha, Xenocs, Grenoble, France) at the Niels Bohr Institute (University of Copenhagen, Copenhagen, Denmark). Additional information is provided in the Supporting Information.

2.4.2. Small-angle neutron scattering (SANS)

SANS measurements were performed at the KWS-2 beamline [35] at Maier-Leibnitz Zentrum in Garching (Garching, Germany) on the Syl-IPN and Sqr-IPN series of samples. Samples were measured at four instrument configurations to cover a wide Q range. Q is defined as the magnitude of the momentum transfer (or scattering) vector (\vec{Q}) and is given in Equation (2), where λ is the wavelength of the radiation and θ is half the scattering angle [36].

$$Q = \frac{4\pi \sin \theta}{\lambda} \quad (2)$$

Three sample-detector distances (1.605 m, 7.605 m, and 19.505 m) and three neutron wavelengths (5.15 Å, 10.31 Å, and 19.60 Å) were used. Either measurements at longer sample-detector distances or measurements with longer wavelengths make it possible to access smaller scattering angles, as can be seen in Equation (2). Additional information is provided in the Supporting Information.

2.4.3. Spin-echo SANS (SESANS)

SESANS measurements were performed on the SESANS instrument located at the Reactor Institute Delft, TU Delft (The Netherlands). As opposed to conventional small-angle scattering measurements, which measure scattering intensity as a function Q (Equation (2)), SESANS measures the degree of depolarization as a function of the so-called spin-echo length Z , essentially the length scale over which correlations in scattering length density are probed in the sample. Z is an instrumental quantity which is defined in Equation (3), where c is a constant ($4.6368 \times 10^{-14} \text{ T}^{-1} \text{ m}^{-2}$), λ is the wavelength of the neutron, L is the magnetic field length, B is the strength of the magnetic field, and θ_0 is the angle of the magnetized foil flipper with respect to the neutron beam

Table 2
Equilibrium water content of silicone-hydrogel IPNs as function of hydrogel content.

Hydrogel content	Water content
f_{hydr} (%)	EWC (%)
20	23
26	25
34	33
42	40
51	43

[37].

$$Z = \frac{c\lambda^2 LB \cot \theta_0}{\pi} \quad (3)$$

The SESANS technique has been well described elsewhere [37–39]. In a SESANS measurement, the average polarization of a neutron beam that has passed through a sample is the quantity that is being measured. The polarization of this beam ($P(Z)$) has to be normalized by the original empty beam polarization ($P_0(Z)$). The degree of depolarization is given in Equation (4).

$$\frac{P(Z)}{P_0(Z)} = \exp\{\Sigma_t [G(Z) - 1]\} \quad (4)$$

The total scattering (Σ_t) is the average number of scattering events for a neutron passing through a sample of thickness t , and $G(Z)$ is a correlation function that is related, via an Abel transform, to a Debye-type autocorrelation function $\gamma(r)$ [39–42]. Σ_t is normalized by the square of the neutron wavelength (λ^2) and the sample thickness (t). Therefore, the following quantity has emerged as a useful y-axis for SESANS measurements [39,42].

$$\frac{\Sigma_t}{\lambda^2 t} (G(Z) - 1) = \frac{1}{\lambda^2 t} \ln \left[\frac{P(Z)}{P_0(Z)} \right] \quad (5)$$

The effective thicknesses of the samples used for these measurements could not be well controlled, as flat samples for scattering measurements were cut from curved tubing. The thicknesses were, therefore, calculated from the experimentally measured neutron transmissions and the known absorbance and incoherent cross-sections of the nuclei in the material (including the polymers but excluding D_2O) [43,44]. The scattering transmission (T) can be related to the scattering power (τ), which is in turn related to the sample thickness (d) and the scattering cross-section per sample volume (Σ), by the following relationship [45].

$$T = \exp(-\tau) \equiv \exp(-d \cdot \Sigma) \quad (6)$$

The thicknesses that are calculated in this way (Table 3) are reasonable for the anticipated thickness of the IPNs.

The SESANS measurements were performed using a monochromatic beam with a theoretical Z ranging from 5 nm to 20 μm [37]. To perform a scan of spin-echo length Z the magnetic field B is varied and different Z measured point-by-point. In the configuration used for these measurements, a range from about 28 nm to 16.3 μm was covered.

Three samples of Sqr-IPNs (Sqr-20, Sqr-36, and Sqr-51) and one sample of Syl-IPN (Syl-22) were studied. They were placed in a cuvette filled with D_2O prior to measurement and allowed to reach EWC before measurements.

$G(Z)$ can be related to the scattering cross section per unit volume $I(Q)$ encountered in a conventional SAS measurement, as shown in Equation (7). $J_0(x)$ is the zeroth order cylindrical Bessel function.

$$G(Z) = \frac{\lambda^2 t}{2\pi \Sigma_t} \int_0^\infty J_0(QZ) I(Q) Q dQ \quad (7)$$

The data for the primary objects were fit using a spherical form factor, which, in Q -space, is given by Equation (8), where R is the sphere radius [46]. This does not necessarily mean that the objects are discrete spheres, but rather that the overall structure can formally be represented well by spherical subunits.

$$I(Q, R) = \frac{4}{3} \pi R^3 \Delta \rho^2 \left[3 \frac{\sin(QR) - QR \cos(QR)}{(QR)^3} \right]^2 \quad (8)$$

The distribution in particle size was included by convoluting the form factor with a size distribution function, as given generally by Equation (9), where $f(R, R', \sigma)$ is the size distribution function [47].

$$I(Q) = \int_0^\infty f(R, R', \sigma) I(Q, R') dR' \quad (9)$$

For the data studied here, a Schulz distribution [48] with mean radius R and width of the size distribution σ was used, which has been shown to be appropriate for many colloidal systems [49]. It was necessary to include a structure factor to satisfactorily fit the data. As the spherical regions are not well-defined, an analytical solution to the structure factor is not suitable, and instead, the numerical method of Robertus *et al.* is used [50]. The data in this study can be well fit if “stickiness parameter” τ_{nm} is set equal to a large value (99), and in this instance, the interparticle interaction is solely as hard spheres. Samples with the lowest concentrations of hydrogel (Sqr-20, Syl-22) could be fit as dilute spheres without invoking a structure factor. However, to ensure consistency and satisfactory fits to the data, the volume fraction was set to a low value (0.01) and the data fit using this same model.

To account for correlations over even longer length scales, a further contribution to the SESANS signal was introduced for all samples, using the Debye–Anderson–Brumberger (DAB) model [51], also known as the Debye–Büchle model [52]. This represents very long-range scattering length density fluctuations in the materials. The DAB model describes a randomly distributed two-phase system and is given by Equation (10).

$$I(Q) = \text{scale} \cdot \frac{\xi^3}{(1 + (Q \cdot \xi)^2)^2} \quad (10)$$

The correlation length (ξ) is the only structural parameter in Equation (10).

The SASfit software package was used for fitting the SESANS data [42,53,54]. The appropriate transformation from Q -space to real-space is performed in the software and was integrated over a finite Q range, defined by the maximum Q of the detector of the instrument ($0 < Q < 0.052 \text{ \AA}^{-1}$).

3. Results

The IPNs studied here are composed of multiple components: the silicone elastomer, silica filler particles, hydrophilic hydrogel, and solvating water. This is already a complex system, but it is further complicated by the many variables that could impact the final structure, such as diffusion rates of monomers into the silicone during production, cross-linking density, silicone type (hardness and shape), and type of filler. This means that it is challenging to determine the overall structure from a single measurement alone. Multiple techniques, as well as multiple contrasts (different types of radiation or labeling) using a single technique, are necessary to improve the ability to highlight the different components. Our goal is to develop tools that can be used regardless of the material complexity to reveal the morphology of the IPNs.

3.1. Microscopy visualizes the hydrogel structure

Inspired by previous attempts to determine the degree of homogeneity or heterogeneity of these IPNs, we used AFM to visualize the surface. Our AFM images show that there are structures that are greater than 10s of nm but smaller than a μm . We performed two types of measurements on the surface of a single IPN (Syl-22). We imaged the surface under dry conditions using normal AFM, and we performed forcemapping in water to measure the surface forces and the hydrophobicity of the sample surface. Fig. 2 shows a set of AFM images of the dry surface. Fig. 2(A) shows the surface features and Fig. 2(B) shows the

Table 3

Experimentally measured neutron transmissions (T) and calculated sample thicknesses (d).

Sample	T	d (cm)
Syl-22	0.486	0.170
Sqr-20	0.648	0.103
Sqr-34	0.715	0.0766
Sqr-51	0.586	0.117

phase image of the same area. Contrast in the phase image typically relates differences in energy dissipation in the AFM recording. Differences in energy dissipation are linked to different surface properties. This could be hardness, stickiness, or hydrophobicity.

The AFM image shows that there really are two distinct components on the surface of the IPN. One is smooth and gives rise to strong change in the phase image, and the other has features with a characteristic scale of ~ 10 nm size that does not affect the phase significantly.

This trend is mirrored in the forcemapping (Fig. 3), which shows features that are consistent with the images that were recorded on the dry sample (Fig. 2). There are low areas having high adhesion (Fig. 3) compatible with strong phase shift (Fig. 2) and vice versa for parts that protrude from the surface.

The result agrees with the low (pink) areas being more sticky and the protruding parts (blue) being less sticky. Our interpretation is that the low areas are more hydrophobic than the protruding areas.

These images clearly show that the structure of the IPNs is heterogeneous on the nanometer to micrometer scale. However, as AFM is a surface technique, it is only sensitive to heterogeneities on the surface. The surface technique must be complemented by techniques that can probe the interior of materials to study the bulk structure. That the IPNs are known to phase separate from AFM suggests that this should be informative.

3.2. Scattering quantifies the hydrogel structure

From the AFM micrographs (Fig. 2), it is clear that there are inhomogeneities on the order of hundreds of nanometers in these materials, on the surface at least. To study features throughout the interior, several variants of X-ray and neutron scattering were used. Unfortunately, the more readily accessible and commonly used forms of scattering were unsuitable to studying these materials. The limitations of the techniques will be discussed below.

3.2.1. Small-angle X-ray and neutron scattering measurements

Small-angle X-ray scattering (SAXS) measurements were performed on IPN samples in both their dry and wet states and for different hydrogel concentrations, but these were unable to provide useful information about the distribution of hydrogel. The results from wet and dry samples are broadly the same. The variation in hydrogel concentration also gives rise to only very small (but systematic) changes in the SAXS signal, and the SAXS data from a hydrogel-free sample (Sqr-00) are essentially the same as those containing hydrogel. This was due to silica filler particles that are known to be present in commercial silicones and dominate the scattering [25,55], which can be explained by the much higher X-ray scattering length density of silica (Table 1). SAXS data

obtained for Syl silicones, which do not contain mechanical silica filler, confirm this hypothesis. (Data are discussed in the Supporting Information.)

Small-angle neutron scattering (SANS) measurements were also performed on IPN samples. When H_2O is used to hydrate the hydrogel in the IPN, the SANS data are very similar to the SAXS data. The silica filler particles do scatter significantly over much of the Q range of the measurements, but no one component dominates overall. This makes disentangling the origin of the scattering challenging. The most dilute sample (Sqr-20 H_2O) can be modeled by considering two populations (compact hydrogel objects and silica filler) to be independent species, which because the hydrogel is “dilute” means that there is no structure factor peak as is the case for more concentrated samples (Supporting Information, Fig. S6). Assuming that the scattering from the silica filler is significant at high Q and that the scattering from dilute hydrogel objects at is significant at low Q , a reasonable fit to the data can be obtained (Supporting Information, Fig. S7).

When D_2O is used to hydrate the hydrogel, however, there is significant scattering intensity with a single component dominating. The SANS data are shown in the Supporting Information (Fig. S8), and the curves do not change significantly with hydrogel concentration. The large amount of scattering intensity, resulting from the large contrast between the D_2O -swollen hydrophilic material and D_2O -free hydrophobic material as well as the thickness of the samples means that there is the possibility of multiple scattering. This was confirmed by modeling the scattering from the most dilute sample (Sqr-20) as a dispersion of spheres that scatter multiply. The multiple scattering calculations were performed in accordance with the literature and as implemented in SASfit [45,56,57]. By accounting for multiple scattering, the SANS data could thus be modeled successfully, with hydrogel that is phase separated on a length scale of 10s–100s of nanometers with a wide size distribution. These length scales are on the high limit of what can be studied with SANS, which further limits the ability to quantify them. While multiple scattering is a problem for SANS, it is not a problem for SESANS [58]. This makes the SESANS technique well-suited to studying these materials.

The data from these SANS measurements are different than previous SANS measurements on hydrophilic polymer and silicone IPNs, which found that data could be modeled with correlation lengths on the order of 10 nm [20–22]. Possible multiple scattering is not discussed in these references. The difference in the interpretation of the SANS data between these previous studies and ours could be down to different syntheses, the existence of multiple scattering, or different materials. Multiple scattering is, generally, considered to be insignificant for scattering from polymers [59], and the data that we present in this study, therefore, are an interesting example of a polymer system where

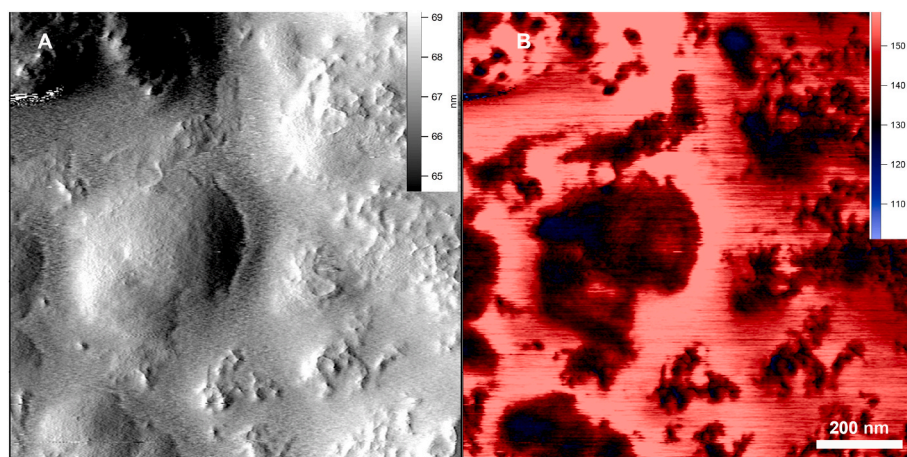


Fig. 2. $1 \times 1 \mu\text{m}^2$ AFM tapping mode image of the surface of Syl-22. (A) Amplitude. (B) Phase.

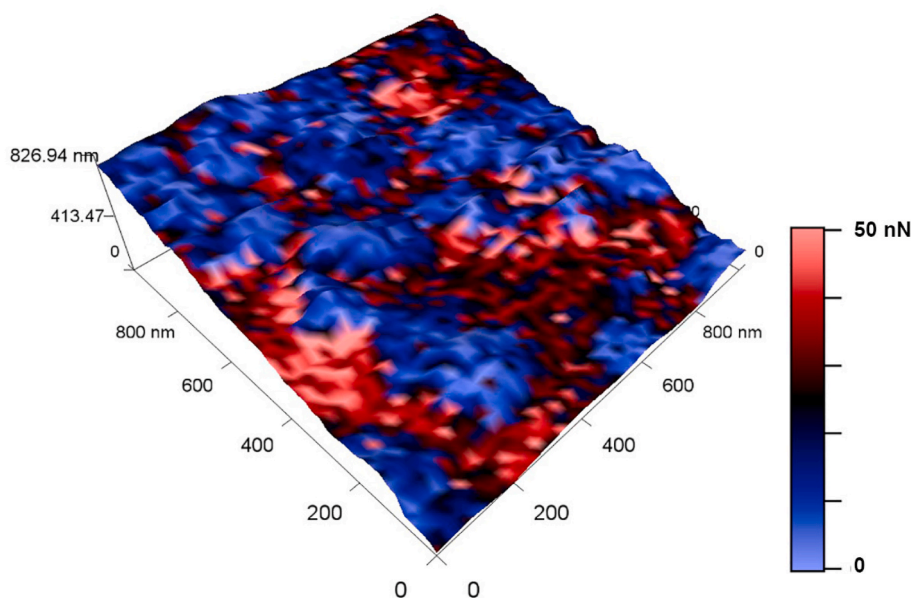


Fig. 3. Force mapping showing the 3D perspective of the topography with adhesion as the color overlay across a $1 \times 1 \mu\text{m}^2$ area of the surface of Syl-22. The color scale for the adhesion is going from light blue (low adhesion) to black (medium adhesion) to pink (strong adhesion). (For interpretation of the references to color in this figure legend, the reader is referred to the Web version of this article.)

multiple scattering cannot be discounted. This is because the IPNs that we report in this study, despite being made up of polymers and D_2O , consist of large regions that have a high scattering power, exactly the conditions that will result in a large degree of multiple scattering [45]. Multiple scattering impacts the low Q part of the SANS data (long length scales) whereas the high Q part is not impacted, and the SANS data shows that there are no significant structures on shorter length scales (from 1 to 20 nm).

3.2.2. Spin-echo small-angle neutron scattering measurements

The main interest is to study the structure of the hydrogel in the Sqr IPN, and as SAXS and SANS are unsuitable for this for the reasons discussed above, the SESANS technique was used. However, to determine if any of the observed structural features are related to the structure of the filler particles in the Sqr samples, the Syl-22 sample was also studied

with SESANS. The data from Syl-22 and Sqr-20 are displayed in Fig. 4. The left panel of the figure shows the SESANS signal up to spin-echo lengths of $2.7 \mu\text{m}$. Over this Z range, the SESANS signal is almost completely dominated by the compact hydrogel objects, as can be seen by the nearly complete overlap of the grey dashed line (compact objects) and black line (total). The curves for the two samples look qualitatively similar, with a rapid depolarization followed by a rather flat plateau for spin-echo lengths greater than around $0.5 \mu\text{m}$. However, the depolarization is more rapid for Syl-20 than Sqr-22 and plateaus at significantly shorter spin-echo lengths.

The SESANS signal varies when structures are present over that length scale, and it is constant when there are not. The rapid depolarization followed by a flattening thus suggests that there are only structures at length scales up to about $0.5 \mu\text{m}$ but nothing larger. However, on closer inspection, the curves are not actually a flat plateau. To study this

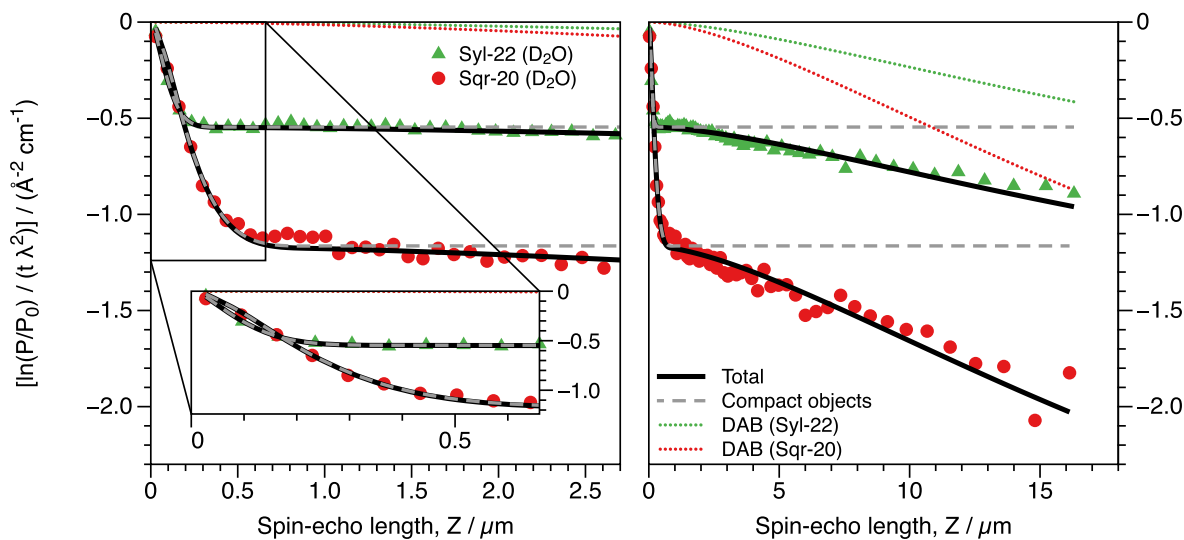


Fig. 4. Comparison of SESANS data from D_2O -hydrated Sqr-20 and Syl-22 samples. The solid lines show fits to both components (compact hydrogel objects and long-range inhomogeneities) whereas the dashed lines show the contribution from the hydrogel objects only and the dotted lines show the contribution from the long-range inhomogeneities only. Left and right panels show data up to spin-echo lengths of 2.7 and $18 \mu\text{m}$, respectively.

in more detail, the samples were measured at spin-echo lengths up to $16.3\ \mu\text{m}$ (Fig. 4 right). Looking at the data measured to longer spin-echo lengths the curves are very similar for the two samples, and it is clear that the depolarization curve has not reached a plateau at $0.5\ \mu\text{m}$. The depolarization continues slowly to longer spin-echo lengths, showing that inhomogeneities exist up to the maximum length scale accessible. The scattering from these, shown by the dotted lines in the right hand panel of Fig. 5, is only significant at large Z .

The obtained SESANS data on three of the samples in the Sqr-series are shown in Fig. 5. The left panel of the figure shows the SESANS signal up to spin-echo lengths of $2.7\ \mu\text{m}$. The data for all samples follow the same overall trend with a rapid depolarization up to spin-echo lengths of about $0.5\ \mu\text{m}$ followed by a much slower depolarization in the entire probed range of spin-echo lengths. On closer inspection, the curves for the more concentrated samples, Sqr-36 and Sqr-51 have a local minimum in the data at $\sim 0.5\ \mu\text{m}$. This can mathematically be accounted for as a structure factor, representing a non-random distribution of the scattering regions. Over this Z range, the scattering is nearly completely dominated by the hydrogel, as can be seen by the overlapping grey dashed lines (compact objects) and solid black line (total).

As described in the Experimental Section, the SESANS data from the compact hydrogel objects were modeled as spheres with a Schulz size distribution plus an additional (DAB) term to take correlations at longer length scales into account. A hard-sphere structure factor was included in the fit of the Sqr-36 and Sqr-51 data but was not necessary for the two low-concentration samples. This is probably not a reflection of different interactions in the samples but just a consequence of the relative low concentration in Sqr-20 and Syl-22. Although a model of discrete spheres are used to fit the data, this does not mean that the structures should be considered to be isolated spheres. Rather, the structure of the IPN at this length scale is a phase-separated, two-phase system that can be represented by spherical subunits, as described above.

The parameters from the fits of the SESANS data are displayed in Table 4. For the two low-concentration samples, the width of the size distribution is very large and uncertain, and this parameter in particular is poorly determined. This is because there is no clear structure factor peak in the data, and therefore, the best fit value is somewhat ambiguous. Furthermore, to avoid undue computational complexity, there are a finite number of points in the Schulz size distribution used for these calculations, which may introduce uncertainty from bin selection. The fit results should thus not be taken as accurate measures of the sizes of

Table 4

Best fit parameters for the compact hydrogel objects of the SESANS data for the D_2O -hydrated Sqr and Syl IPNs. R is mean value of the sphere radius, and σ is the width of the Schulz distribution. All samples were fit with a hard ($\tau = 99$ fixed) sphere structure factor according to the Robertus model, where ϕ denotes the volume fraction of the hydrogel objects.

Sample	R/nm	σ	ϕ
Syl-22	40	0.7	0.01*
Sqr-20	90	0.8	0.01*
Sqr-36	240	0.5	0.51
Sqr-51	370	0.4	0.63

* Fixed to this value as the spheres were too dilute to fit this parameter with precision.

the hydrogel domains, but rather an estimate. For both Sqr-20 and Syl-22 the modeling results in spheres with a radius on the order of 10s of nm and a very wide size distribution. For higher hydrogel concentrations the structure factor term helps to stabilize the modeling. The model results in sphere radii of a few hundred nm and a broad size distribution.

4. Discussion

The combination of an imaging technique (AFM) and a scattering technique (SESANS) has revealed the formation of hierarchical hydrogel domains in these IPNs with length scales up to more than 100 nm. Using D_2O as a swelling and contrast agent for SESANS was essential to study the water-swollen structure of the IPN. The silicone in the Sqr series clearly contains filler particles, determined from X-ray scattering measurements, where filler dominates the scattering as it has been also observed elsewhere [25,55]. This silicone is medical grade and is, therefore, highly relevant for application in medical devices.

From a consideration of the density fluctuations observed by SESANS and the inhomogeneities imaged by AFM, we can draw several conclusions about the structure of these hydrophilic-hydrophobic IPNs. There are regions of hydrophilic and hydrophobic polymer interpenetrating on a length scale on the order of 100s of nanometers. Therefore, the schematics of a two-phase system that were used to demonstrate the contrast in scattering experiments in Fig. 1 are broadly correct. These, however, do not fill the material homogeneously, and on larger length scales (100s of nanometers to 10s of micrometers), there are density fluctuations with more hydrogel-rich and more hydrogel-poor regions. These may arise from the cross-linked nature of the silicone host polymer or may

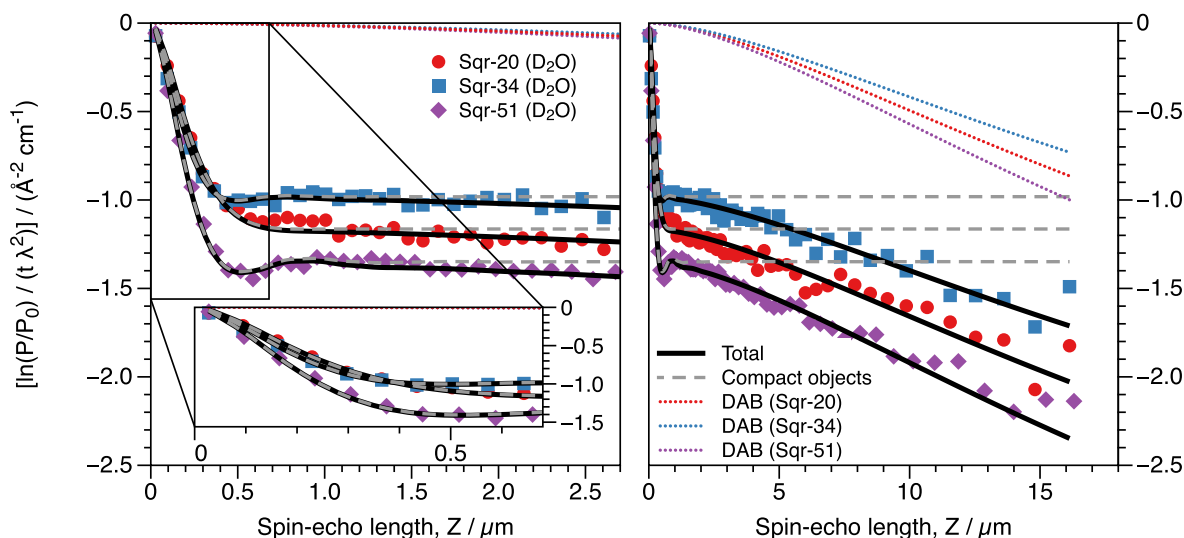


Fig. 5. SESANS data of different D_2O -hydrated Sqr samples. The solid lines show fits to both components (compact hydrogel objects and long-range inhomogeneities), whereas the dashed lines show the contribution from the hydrogel objects only and the dashed dotted show the contribution from the long-range inhomogeneities only. Left and right panels show data up to spin-echo lengths of 2.7 and $18\ \mu\text{m}$, respectively.

arise from the polymerization kinetics of the guest polymer. From these data, it is not possible to say. Despite these density fluctuations, the hydrogel does form a system spanning network, although this could not be proven from the scattering data alone. For example, McGarey et al. used the diffusion of KCl through their IPN membranes to prove this [60]. For the studied IPNs in this study, it has been already shown elsewhere through dye diffusion and drug release experiments that the hydrophilic domains are connected in bulk and with the surface [7–9].

All the neutron scattering contrasts and techniques give a consistent description of the structure of the IPN with the lowest concentration of hydrogel. We assume that the same would be true for higher concentrations, if data could all be fully analyzed. They consist of large (10s–100s on nanometers) phase separated regions of hydrogel and silicone. The compact hydrogel objects can be modeled as spheres with a broad distribution, which are distributed as noninteracting hard spheres when sufficiently concentrated. The reciprocal space SANS measurements suffer from multiple scattering, and furthermore, the largest sizes in the structure are not accessible with conventional SANS. This makes determining the structure from SANS alone impossible. When H₂O is used to hydrate the hydrogel, the hydrophilic regions have insufficient contrast with the remaining material, and the scattering is too complicated to model. When D₂O is used to hydrate the hydrogel, the hydrophilic regions now have too high a scattering power, and the resulting multiple scattering means that analyzing the data unambiguously becomes problematic. Real space SESANS measurements, on the other hand, provide a way of quantitatively determining the structure of the materials. Data are obtained over a broad range of length scales (up to 16 µm), and the multiple scattering arising from the high scattering power is simply addressed in the data modeling.

Given the insight into these structures that have been obtained using techniques from neutron scattering, SESANS in particular, it is immediately clear that these IPNs in commercial Sqr and Syl silicones have a very hierarchical structure with potentially important structures at all these length scales. The results from both Sqr and Syl IPNs show that, despite the length scales of these features being broadly similar, the precise size is dependent on the host silicone polymer. This seems to impact the feature size more than the concentration of guest hydrogel polymer, which, aside from impacting concentration dependent parameters (scale and structure factor), does not significantly impact the structures.

5. Conclusions

The structural complexity of these hydrophilic-hydrophobic IPNs demanded the use of many analytical techniques, with AFM and SESANS proving particularly informative. We find these IPN materials to consist of locally phase-separated and interpenetrating regions of hydrogel and silicone on the nanometer scale, which presumably provides a large amount of surface area between the hydrophilic and hydrophobic polymers. This way of modeling data differs from other neutron scattering data analyzed by others from similar IPNs, and it may be important for characterizing these specific IPNs for their desired application.

The domains of hydrogel are likely to be the origin of the biomedically advantageous properties of these IPNs. The patches of hydrogel identified at the interface make an unfavorable surface for bacterial adsorption, and the regions of hydrogel in the bulk provide a route for drug molecules to diffuse through. Interactions at the silicone-hydrogel interface within the material, in particular, will determine how different drugs, which differ in their degrees of hydrophobicity and hydrophilicity, diffuse through the IPNs. Determining the size and concentration of regions of hydrogel will improve the understanding of this process. IPNs synthesized in commercial, medical-grade silicones also contain fractal silica particles (as clearly observed by SAXS), which necessitated the use of D₂O hydration to study the hydrogel structure using SANS and SESANS. The fillers impact the macroscopic properties

of the materials, but it is not clear whether or not these fillers impact the structure of the hydrogel or the diffusion of molecules, although it might be speculated that they do. These IPNs are clearly highly complex and structured.

The determination of the structure of materials is, of course, interesting, but it is finding what can be done with this information that will be crucial for the development of future medical devices. The identification of the important length scales and the important structures is a promising start. Future work should help reveal how the material properties relate to the structural parameters as well as what structures and what dimensions are the important ones for the properties of the materials and their clinical application. Overcoming the negative health outcomes arising from urinary tract infections by avoiding them through infection-resistant devices and treating them with targeted drug delivery justifies this effort. In tandem with advances in the use of these devices in the clinical setting, structural measurements will be highly valuable.

CRedit author contribution statement

Gregory N. Smith: Formal analysis, Investigation, Writing – original draft. **Erik Brok:** Conceptualization, Methodology, Formal analysis, Investigation, Writing – review & editing, Visualization. **Martin Schmiele:** Conceptualization, Methodology, Formal analysis, Writing – review & editing, Visualization. **Kell Mortensen:** Conceptualization, Formal analysis, Supervision, Writing – review & editing. **Wim G. Bouwman:** Methodology, Formal analysis, Investigation, Writing – review & editing. **Chris P. Duif:** Methodology, Investigation, Data curation, Writing – review & editing. **Tue Hassenkam:** Conceptualization, Methodology, Formal analysis, Investigation, Data curation, Writing – review & editing, Visualization. **Martin Alm:** Conceptualization, Resources, Writing – original draft. **Peter Thomsen:** Resources, Writing – review & editing, Funding acquisition. **Lise Arleth:** Conceptualization, Writing – review & editing, Supervision, Project administration, Funding acquisition.

Declaration of competing interest

The authors declare that they have no known competing financial interests or personal relationships that could have appeared to influence the work reported in this paper.

Acknowledgements

This work is partly funded by the Innovation Fund Denmark (IFD) as part of project Linking Industry to Neutrons and X-rays (LINX) under File No. 5152-00005B. We thank the Danish Agency for Science, Technology, and Innovation for funding the instrument center DanScatt. The authors gratefully acknowledge the assistance of Dr Aurel Radulescu (Maier-Leibnitz Zentrum, Garching) with performing the SANS experiments. The authors also acknowledge Dr Joachim Kohlbrecher (Paul Scherrer Institute, Switzerland) for valuable discussions regarding the multiple scattering and the SASfit software, including providing bespoke versions to enable fitting for this study.

Appendix A. Supplementary data

Supplementary data to this article can be found online at <https://doi.org/10.1016/j.polymer.2021.123671>.

References

- [1] H.H. Tuson, D.B. Weibel, Bacteria-surface interactions, *Soft Matter* 9 (2013) 4368–4380.
- [2] F.M. Fowkes, Additivity of intermolecular forces at interfaces. I. Determination of the contribution to surface and interfacial tensions of dispersion forces in various liquids, *J. Phys. Chem.* 67 (1963) 2538–2541.

- [3] A.S. Hoffman, Hydrogels for biomedical applications, *Adv. Drug Deliv. Rev.* 64 (2012) 18–23.
- [4] A. Vedadghavami, F. Minooei, M.H. Mohammadi, S. Khetani, A. Rezaei Kolahchi, S. Mashayekhan, A. Sanati-Nezhad, Manufacturing of hydrogel biomaterials with controlled mechanical properties for tissue engineering applications, *Acta Biomater.* 62 (2017) 42–63.
- [5] J.V. Alemán, A.V. Chadwick, J. He, M. Hess, K. Horie, R.G. Jones, P. Kratochvíl, I. Meisel, I. Mita, G. Moad, S. Penczek, R.F.T. Stepto, Definitions of terms relating to the structure and processing of sols, gels, networks, and inorganic-organic hybrid materials (IUPAC Recommendations 2007), *Pure Appl. Chem.* 79 (2007) 1801–1829.
- [6] D. Myung, D. Waters, M. Wiseman, P. Duhamel, J. Noolandi, C.N. Ta, C.W. Frank, Progress in the development of interpenetrating polymer network hydrogels, *Polym. Adv. Technol.* 19 (2008) 647–657.
- [7] S.L. Steffensen, M.H. Vestergaard, E.H. Møller, M. Groenning, M. Alm, H. Franzky, H.M. Nielsen, Soft hydrogels interpenetrating silicone – a polymer network for drug-releasing medical devices, *J. Biomed. Mater. Res., Part B* 104B (2015) 402–410.
- [8] S.L. Steffensen, M.H. Vestergaard, M. Groenning, M. Alm, H. Franzky, H. M. Nielsen, Sustained prevention of biofilm formation on a novel silicone matrix suitable for medical devices, *Eur. J. Pharm. Biopharm.* 94 (2015) 305–311.
- [9] S. Mohanty, M. Alm, M. Hemmingsen, A. Dolatshahi-Pirouz, J. Trifol, P. Thomsen, M. Dufva, A. Wolff, J. Enneus, 3D printed silicone-hydrogel scaffold with enhanced physicochemical properties, *Biomacromolecules* 17 (2016) 1321–1329.
- [10] M. Stenger, K. Klein, R.B. Grønnemose, J.K. Klitgaard, H.J. Kolmos, J.S. Lindholt, M. Alm, P. Thomsen, T.E. Andersen, Co-release of dicloxacillin and thioridazine from catheter material containing an interpenetrating polymer network for inhibiting device-associated *Staphylococcus aureus* infection, *J. Contr. Release* 241 (2016) 125–134.
- [11] L. Riber, M. Burmølle, M. Alm, S.M. Milani, P. Thomsen, L.H. Hansen, S. J. Sørensen, Enhanced plasmid loss in bacterial populations exposed to the antimicrobial compound irgasan delivered from interpenetrating polymer network silicone hydrogels, *Plasmid* 87–88 (2016) 72–78.
- [12] K. Klein, R.B. Grønnemose, M. Alm, K.S. Brinch, H.J. Kolmos, T.E. Andersen, Controlled release of plectasin n2114 from a hybrid silicone-hydrogel material for inhibition of *staphylococcus aureus* biofilm, *Antimicrob. Agents Chemother.* 61 (2017) 1–6.
- [13] O.R. Davies, A.L. Lewis, M.J. Whitaker, H. Tai, K.M. Shakesheff, S.M. Howdle, Applications of supercritical CO₂ in the fabrication of polymer systems for drug delivery and tissue engineering, *Adv. Drug Deliv. Rev.* 60 (2008) 373–387.
- [14] J. Peach, J. Eastoe, Supercritical carbon dioxide: a solvent like no other, *Beilstein J. Org. Chem.* 10 (2014) 1878–1895.
- [15] M. Ghani, A. Heiskanen, J. Kajtez, B. Rezaei, N.B. Larsen, P. Thomsen, A. Kristensen, A. Žukauskas, M. Alm, J. Emnéus, On-demand reversible uv-triggered interpenetrating polymer network-based drug delivery system using the spiropyran–merocyanine hydrophobicity switch, *ACS Appl. Mater. Interfaces* 13 (2021) 3591–3604.
- [16] M. Ghani, A. Heiskanen, P. Thomsen, M. Alm, J. Emnéus, Molecular-gated drug delivery systems using light-triggered hydrophobic-to-hydrophilic switches, *ACS Appl. Bio Mater.* 4 (2021) 1624–1631.
- [17] J.W. Warren, Catheter-associated urinary tract infections, *Int. J. Antimicrob. Agents* 17 (2001) 299–303.
- [18] G. Williams, D. Stickler, Some observations on the diffusion of antimicrobial agents through the retention balloons of Foley catheters, *J. Urol.* 178 (2007) 697–701.
- [19] M.H. Alm, Impregnation and Surface Modification of Polymers in Liquid and Supercritical Carbon Dioxide, Ph.D. thesis, Roskilde University, 2007.
- [20] J.H. An, A.M. Fernandez, L.H. Sperling, Development of multiphase morphology in poly(cross-butadiene)-inter-poly(cross-styrene) interpenetrating polymer networks, *Macromolecules* 20 (1987) 191–193.
- [21] B. McGarey, R.W. Richards, The size of phase separated regions in poly (dimethylsiloxane) polystyrene sequential interpenetrating networks determined by small-angle neutron-scattering, *Polymer* 27 (1986) 1315–1324.
- [22] B. McGarey, R.W. Richards, Phase separated zone dimensions in water swollen polydimethylsiloxane polymethacrylic acid interpenetrating networks, *Br. Polym. J.* 19 (1987) 111–117.
- [23] J. Lal, J.M. Widmaier, J. Bastide, F. Boue, Determination of an interpenetrating network structure by small-angle neutron scattering, *Macromolecules* 27 (1994) 6443–6451.
- [24] M. Song, D.J. Hourston, F.U. Schafer, A study of the morphology of polyurethane-polystyrene interpenetrating polymer networks by means of small angle X-ray scattering, modulated-temperature differential scanning calorimetry, and dynamic mechanical thermal analysis techniques, *J. Appl. Polym. Sci.* 79 (2001) 1958–1964.
- [25] A. Hillerström, M. Andersson, J.S. Pedersen, A. Altskär, M. Langton, J. van Stam, B. Kronberg, Transparency and wettability of PVP/PDMS-IPN synthesized in different organic solvents, *J. Appl. Polym. Sci.* 114 (2009) 1828–1839.
- [26] V.N. Pavlyuchenko, O.V. Sorochinskaya, S.S. Ivanchev, S.Y. Khaikin, V.A. Trounov, V.T. Lebedev, E.A. Sosnov, I.V. Gofman, New silicone hydrogels based on interpenetrating polymer networks comprising polysiloxane and poly(vinyl alcohol) networks, *Polym. Adv. Technol.* 20 (2009) 367–377.
- [27] F. Abbasi, H. Mirzadeh, A.A. Katbab, Sequential interpenetrating polymer networks of poly(2-hydroxyethyl methacrylate) and polydimethylsiloxane, *J. Appl. Polym. Sci.* 85 (2002) 1825–1831.
- [28] R.K. Bose, K.K.S. Lau, Mechanical properties of ultrahigh molecular weight PHEMA hydrogels synthesized using initiated chemical vapor deposition, *Biomacromolecules* 11 (2010) 2116–2122.
- [29] A. Voit, A. Krekhov, W. Enge, L. Kramer, W. Köhler, Thermal patterning of a critical polymer blend, *Phys. Rev. Lett.* 94 (2005) 214501.
- [30] G.N. Smith, I. Grillo, S.E. Rogers, J. Eastoe, Surfactants with colloids: Adsorption or absorption? *J. Colloid Interface Sci.* 449 (2015) 205–214.
- [31] CRC, Standard density of water, in: *CRC Handbook of Chemistry and Physics*, 76th ed., CRC Press, 1995.
- [32] CRC, Density of D₂O, in: *CRC Handbook of Chemistry and Physics*, 76th ed., CRC Press, 1995.
- [33] O. Mageli, C.S. Sheppard, *Organic Peroxides*, vol. 1, Wiley-Interscience, New York, 1970.
- [34] R. Hiatt, *Organic Peroxides*, vol. 2, Wiley-Interscience, New York, 1971.
- [35] A. Radulescu, V. Pipich, H. Frielinghaus, M.S. Appavou, KWS-2, the high intensity/wide Q-range small-angle neutron diffractometer for soft-matter and biology at FRM II, *J. Phys.: Conf. Ser.* 351 (2012), 012026.
- [36] I. Grillo, Small-angle neutron scattering and applications in soft condensed matter, in: R. Borsali, R. Pecora (Eds.), *Soft Matter Characterization*, Springer Netherlands, 2008, pp. 723–782, https://doi.org/10.1007/978-1-4020-4465-6_13.
- [37] M.T. Rekveldt, J. Plomp, W.G. Bouwman, W.H. Kraan, S. Grigoriev, M. Blaauw, Spin-echo small angle neutron scattering in delft, *Rev. Sci. Instrum.* 76 (2005), 033901.
- [38] M.T. Rekveldt, Novel sans instrument using neutron spin echo, *Nucl. Instrum. Methods Phys. Res., Sect. B* 114 (1996) 366–370.
- [39] A.L. Washington, X. Li, A.B. Schofield, K. Hong, M.R. Fitzsimmons, R. Dalglish, R. Pynn, Inter-particle correlations in a hard-sphere colloidal suspension with polymer additives investigated by spin echo small angle neutron scattering (SESANS), *Soft Matter* 10 (2014) 3016–3026.
- [40] R. Andersson, L.F. van Heijkamp, I.M. de Schepper, W.G. Bouwman, Analysis of spin-echo small-angle neutron scattering measurements, *J. Appl. Crystallogr.* 41 (2008) 868–885.
- [41] S.R. Parnell, A.L. Washington, A.J. Parnell, A. Walsh, R.M. Dalglish, F. Li, W. A. Hamilton, S. Prevost, J.P.A. Fairclough, R. Pynn, Porosity of silica Stober particles determined by spin-echo small angle neutron scattering, *Soft Matter* 12 (2016) 4709–4714.
- [42] J. Kohlbrecher, A. Studer, Transformation cycle between the spherically symmetric correlation function, projected correlation function and differential cross section as implemented in SASfit, *J. Appl. Crystallogr.* 50 (2017) 1395–1403.
- [43] H. Rauch, W. Waschkowski, *Neutron Data Booklet* (Institut Laue–Langevin), second ed., OCP Science, Philadelphia, 2003, 1.1–1.1.1–1.1.17.
- [44] V.F. Sears, *International Tables for Crystallography Volume C: Mathematical, Physical and Chemical Tables*, third ed., Kluwer Academic Publishers, Dordrecht, 2006, pp. 444–454, <https://doi.org/10.1107/97809553602060000103>.
- [45] G.V. Jensen, J.G. Barker, Effects of multiple scattering encountered for various small-angle scattering model functions, *J. Appl. Crystallogr.* 51 (2018) 1455–1466.
- [46] A. Guinier, G. Fournet, *Small-Angle Scattering of X-Rays*, John Wiley & Sons, New York, 1955, <https://doi.org/10.1002/pol.1956.120199326>.
- [47] I. Grillo, Effect of Instrumental Resolution and Polydispersity on Ideal Form Factor in Small Angle Neutron Scattering, ILL Technical Report ILL01GRT08T, Technical Report, Institut Laue Langevin, 2001.
- [48] G.V. Schulz, The kinetics of chain polymerization. V. The effect of various reaction species on the multimolecularity, *Z. Phys. Chem., Abt. B* 43 (1939) 25–46.
- [49] M. Kotlarchyk, S. Chen, Analysis of small angle neutron scattering spectra from polydisperse interacting colloids, *J. Chem. Phys.* 79 (1983) 2461–2469.
- [50] C. Robertus, W.H. Philpess, J.G.H. Joosten, Y.K. Levine, Solution of the Percus–Yevick approximation of the multicomponent adhesive sphere system to the small angle x-ray scattering from microemulsions, *J. Chem. Phys.* 90 (1989) 4482–4490.
- [51] P. Debye, H.R. Anderson, H. Brumberger, Scattering by an inhomogeneous solid. II. The correlation function and its application, *J. Appl. Phys.* 28 (1957) 679–683.
- [52] P. Debye, A.M. Bueche, Scattering by an inhomogeneous solid, *J. Appl. Phys.* 20 (1949) 518–525.
- [53] I. Brähler, J. Kohlbrecher, A.F. Thünemann, SASfit: a tool for small-angle scattering data analysis using a library of analytical expressions, *J. Appl. Crystallogr.* 48 (2015) 1587–1598.
- [54] SASfit, URL, <https://github.com/SASfit/SASfit/>, 2020.
- [55] A. Nakatani, W. Chen, R. Schmidt, G. Gordon, C. Han, Chain dimensions in polysilicate-filled poly(dimethyl siloxane), *Polymer* 42 (2001) 3713–3722.
- [56] J. Schelten, W. Schmatz, Multiple-scattering treatment for small-angle scattering problems, *J. Appl. Crystallogr.* 13 (1980) 385–390.
- [57] J. Kohlbrecher, User guide for the SASfit software package: A program for fitting elementary structural models to small angle scattering data (April 23, 2020), URL, <https://github.com/SASfit/SASfit/blob/master/doc/manual/sasfit.pdf>, 2020.
- [58] C. Rehm, J. Barker, W.G. Bouwman, R. Pynn, DCD USANS, SESANS, A comparison of two neutron scattering techniques applicable for the study of large-scale structures, *J. Appl. Crystallogr.* 46 (2013) 354–364.
- [59] P. Goyal, J. King, G. Summerfield, Multiple scattering in small-angle neutron scattering measurements on polymers, *Polymer* 24 (1983) 131–134.
- [60] B. McGarey, A.D.W. McLenaghan, R.W. Richards, Guest network co-continuity in interpenetrating polymer networks - a diffusion study, *Br. Polym. J.* 21 (1989) 227–232.

Supplementary Material—The structure of interpenetrating polymer networks (IPNs) for medical devices with reduced risk of infection

Gregory N. Smith^{a,b,*}, Erik Brok^b, Martin Schmiele^b, Kell Mortensen^b, Wim G. Bouwman^c, Chris P. Duif^c, Tue Hassenkam^d, Martin Alm^e, Peter Thomsen^e and Lise Arleth^b

^aCurrent address: ISIS Neutron and Muon Source, Science and Technology Facilities Council, Rutherford Appleton Laboratory, Didcot, OX11 0QX, United Kingdom

^bNiels Bohr Institute, University of Copenhagen, Universitetsparken 5, 2100 Copenhagen Ø, Denmark

^cFaculty of Applied Sciences, Delft University of Technology, 2629 JB Delft, The Netherlands


^dDepartment of Chemistry, University of Copenhagen, Universitetsparken 5, 2100 Copenhagen Ø, Denmark

^eBioModics ApS, 2610 Rødovre, Denmark

ABSTRACT

Additional information on scattering models used; SAXS data; SANS and SESANS data on H₂O-hydrated and D₂O-hydrated IPNs

*Corresponding author

 gregory.smith@stfc.ac.uk (G.N. Smith)

ORCID(s): 0000-0002-0074-5657 (G.N. Smith); 0000-0003-4377-8747 (E. Brok); 0000-0001-6973-3155 (M. Schmiele); 0000-0002-8998-939089 (K. Mortensen); 0000-0002-5331-8085 (W.G. Bouwman); 0000-0002-3263-963X (C.P. Duif); 0000-0002-2184-3360 (T. Hassenkam); 0000-0003-4991-4519 (M. Alm); 0000-0002-1183-8795 (P. Thomsen); 0000-0002-4694-4299 (L. Arleth)

S1. Small-angle X-ray scattering (SAXS)

S1.1. Measurements

SAXS experiments were performed with a lab-based micro-focus SWAXS camera (Ganesha, Xenocs, Grenoble, France) at the Niels Bohr Institute. The source, a 30 W X-ray microfocus source (Genix 3D, Xenocs, Sassenage, France), is followed by an evacuated collimation system consisting of two automated double slit systems (JJ X-Ray A/S, Hørsholm, Denmark), separated by the collimation length of 119 cm, and an evacuated detector tank. Aperture sizes were $0.5 \times 0.5 \text{ mm}^2$ for the source-sided tungsten blades and $0.2 \times 0.2 \text{ mm}^2$ for the sample-sided scatterless silicon blades. This provides an X-ray photon flux of about $1.2 \cdot 10^6 \text{ ph/s}$ at the Cu K_α wavelength of $\lambda = 1.5418 \text{ \AA}$ at the sample position in the evacuated detector tank. The X-ray scattering patterns were recorded with a 2D Pilatus 300K detector (Dectris AG, Baden, Switzerland) with a pixel size of $172 \text{ }\mu\text{m}$. The beam centers and the sample-detector distance of 1465 mm were calibrated using a silver behenate standard. The 2D scattering patterns were azimuthally averaged and the scattering angles (2θ) were converted to a Q -scale via $Q = (4\pi/\lambda) \sin(2\theta/2)$, giving a Q -range of 0.003 to 0.3 \AA^{-1} . The scattered intensity $I(Q)$ was corrected for sample transmission, thickness and exposure time and is provided in arbitrary units. All measurements were performed at room temperature ($\sim 25^\circ\text{C}$).

S1.2. Model for filler structure (mass-surface fractal)

For SAXS data of the dry and hydrated Sqr-IPN samples, the scattering predominantly arises from the silica filler particles, Table 1. The filler is assumed to consist of aggregates of primary particles with an internal structure that can be described as a surface fractal. This scattering is modeled by the mass-surface fractal model described below. The same model is used to account for a small contribution to the scattering from filler particles at high- Q in the SANS data of the D_2O -soaked Sqr-IPN samples and is added to the DAB model. The scattering patterns can be divided into two different Q -regions where the intensity follows power laws in Q ($I \propto Q^{-n}$). For mass fractals n is $1 < n < 3$ and for surface fractals $3 < n < 4$. The exponent n relates to the fractal dimension of a surface fractal (D_s) and a mass fractal (D_m) according to Equation S1 [?].

$$n = \begin{cases} D_m & \text{for mass fractals } (1 < D_m < 3) \\ 6 - D_s & \text{for surface fractals } (2 < D_s < 3) \end{cases} \quad (\text{S1})$$

The filler particle structures in silicone are assumed to be similar to fumed silica. The scattering of fumed silica is described in literature by a combined mass-surface fractal structure of the primary silica particles and is given by Equation S2 [? ?].

$$I(Q) = \text{scale} \cdot \left\{ [1 + (Q \cdot a)^2]^{D_m/2} \cdot [1 + (Q \cdot b)^2]^{(6-D_s-D_m)/2} \right\}^{-1} + \text{background} \quad (\text{S2})$$

Here, the scale factor ($N(\Delta\rho)^2V^2$) is calculated from the number concentration (N), volume (V) and the difference in scattering length density between particle and background ($\Delta\rho$) of the primary filler particles. The a and b parameters are given in terms of the radius of gyration of the small primary particles (r_g) and the radius of gyration of the clusters (R_g) according to Equation S3.

$$a = \frac{R_g}{(3D_m/2)^{1/2}}, \quad b = \frac{r_g}{[3(6 - D_s - D_m)/2]^{1/2}} \quad (\text{S3})$$

The first factor in Equation S2 describes the scattering of clusters with a mass fractal structure, which scales for $Q \gg a$ as Q^{-D_m} . The second factor is a correction to the first one, accounting for the scattering of the primary particles assumed to have a surface fractal structure.

Since the total cluster size is greater than can be resolved in the Q range of our scattering measurements, it can only be determined that the clusters (R_g) are large compared to our experimental limitations, or that they are larger than approximately 400 nm.

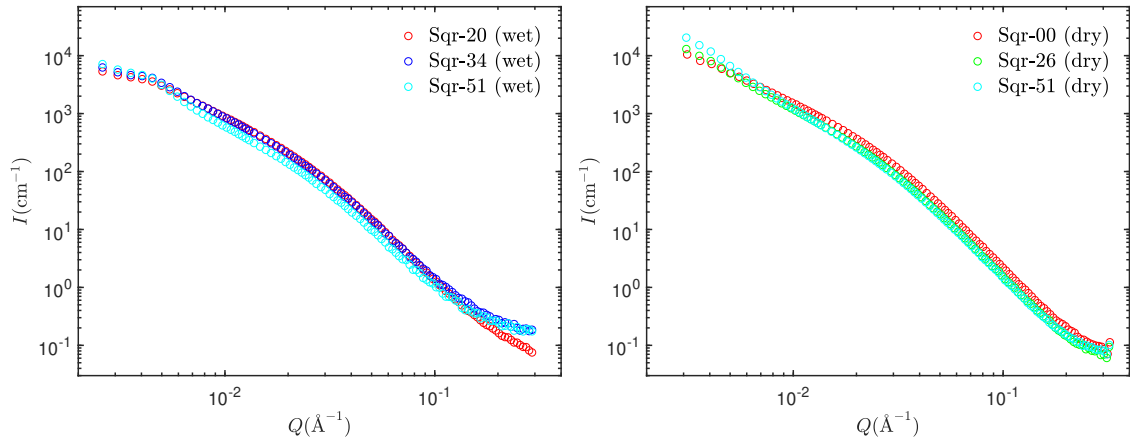


Figure S1: Comparison of SAXS patterns of wet (left) and dry (right) Sqr samples with different hydrogel content.

S1.3. Dry and wet Sqr IPN samples

Figure S2 shows the scattering of a dry and a H₂O-hydrated Sqr-26 sample. Except for the extreme high- and low- Q parts the shape of the two curves are almost identical, which suggests that the same nanostructure gives rise to the measured scattering intensity. The deviation at high- Q can probably be attributed to scattering (background) from differences between the mica windows used in the measurements of the hydrated sample, whereas the difference in scattering at low- Q could be due to the swelling of the sample. Similar observations were made for the entire Sqr series.

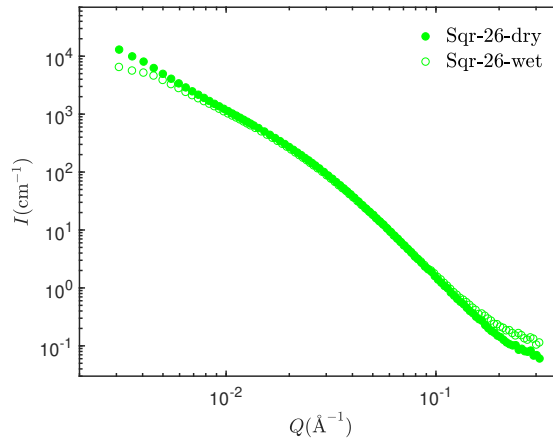


Figure S2: Comparison of SAXS signals from dry and H₂O-hydrated Sqr-26.

The SAXS data of the dry and wet Sqr samples in Figure S3 were modeled with the mass-surface fractal model in Equation S2. The radius of gyration R_g for the clusters was fixed to a sufficiently large size (400 nm) and the one for the primary particles r_g fitted simultaneously for all wet or dry data sets.

There are minor, but systematic differences (Tables S1 and S2), in the fit dimensions of the SAXS on the filler when comparing samples with different amounts of hydrogel and when comparing samples that are either dry or hydrated. The mass and surface fractal dimensions vary as the amount of hydrogel increases, with the mass fractal dimension increasing and the surface fractal dimension decreasing. When comparing the wet and dry samples, an increase of primary particle r_g by ~ 1.25 nm is found, which could relate to the formation of a hydration layer around the silica filler.

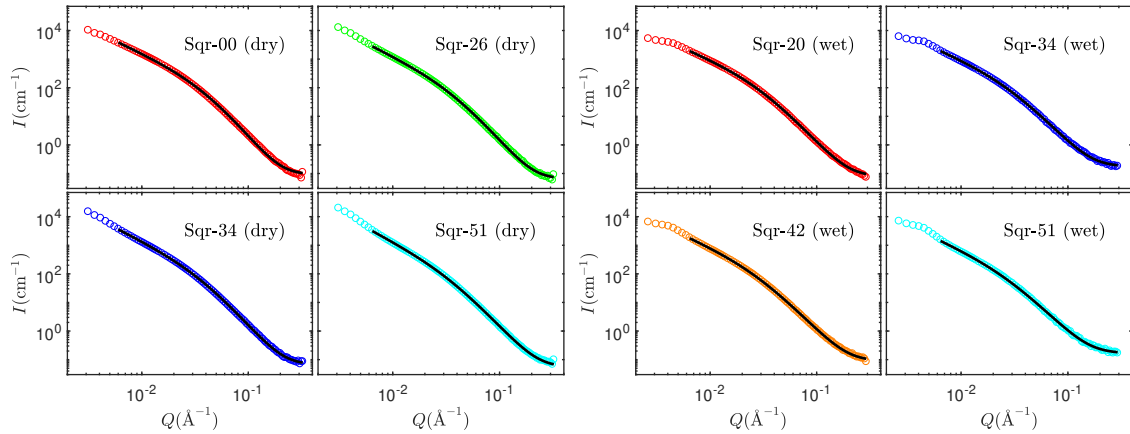


Figure S3: SAXS data of dry (left) and wet Sqr (right) samples with different hydrogel concentrations. Fits with the mass-surface fractal model describe the data very well. The scattering is overall quite similar for the different hydrogel concentrations. The scattering is believed to originate mostly from filler particles.

Sample	Scale (10^4 cm^{-1})	r_g (Å)	R_g (Å)	D_m (-)	D_s (-)	Bkg (cm^{-1})
Sqr-00	43.00 ± 0.18	50.85 ± 0.12	4000	1.736 ± 0.002	1.525 ± 0.009	0.0910 ± 0.0012
Sqr-20	45.52 ± 0.27	50.85 ± 0.12	4000	1.846 ± 0.002	1.692 ± 0.010	0.0638 ± 0.0009
Sqr-26	56.24 ± 0.21	50.85 ± 0.12	4000	1.887 ± 0.001	1.787 ± 0.007	0.0658 ± 0.0009
Sqr-51	71.03 ± 0.27	50.85 ± 0.12	4000	1.992 ± 0.002	1.993 ± 0.006	0.0541 ± 0.0008

Table S1

Best fit parameters for the SAXS patterns of dry Sqr samples, modeled with the mass-surface fractal model. r_g was fitted globally for the whole series.

Sample	Scale (10^4 cm^{-1})	r_g (Å)	R_g (Å)	D_m (-)	D_s (-)	Bkg (cm^{-1})
Sqr-20	18.43 ± 0.17	63.3 ± 0.3	4000	1.609 ± 0.004	1.999 ± 0.009	0.0778 ± 0.0013
Sqr-26	24.01 ± 0.23	63.3 ± 0.3	4000	1.631 ± 0.004	2.023 ± 0.010	0.1153 ± 0.0018
Sqr-34	20.75 ± 0.23	63.3 ± 0.3	4000	1.660 ± 0.004	2.128 ± 0.013	0.1724 ± 0.0029
Sqr-42	21.55 ± 0.19	63.3 ± 0.3	4000	1.714 ± 0.004	2.195 ± 0.008	0.0877 ± 0.0013
Sqr-51	18.78 ± 0.09	63.3 ± 0.3	4000	1.747 ± 0.002	2.294 ± 0.017	0.164 ± 0.004

Table S2

Best fit parameters for the SAXS patterns of wet Sqr samples, modeled with the mass-surface fractal model. r_g was fitted globally for the whole series.

S2. Dry Syl IPN samples

SAXS data on the series of dry Syl samples are shown in Figure S4. There is a dramatic change in scattering between the pure Syl-00 and the hydrogel containing IPN samples, showing that the scattering from the IPN samples is not dominated by scattering from filler particles, but by scattering associated with the hydrogel. The different hydrogel concentrations give rise to similar scattering curves.

S3. Small-angle neutron scattering (SANS)

S3.1. Measurements

SANS measurements were performed at the KWS-2 beamline [?] at Maier–Leibnitz Zentrum in Garching on the Syl-IPN and Sqr-IPN series of samples. The samples containing hydrogel were soaked for one week in either H_2O or D_2O to obtain $EW C$ and the desired contrast. Up to four different experimental setups with the parameters shown in Table S3 were used. Samples soaked in H_2O were measured using all four setups covering a combined Q -range of 0.0008 – 0.48 Å^{-1} . Samples soaked in D_2O were measured in setups 2, 3 and 4, providing a Q -range of 0.0013 –

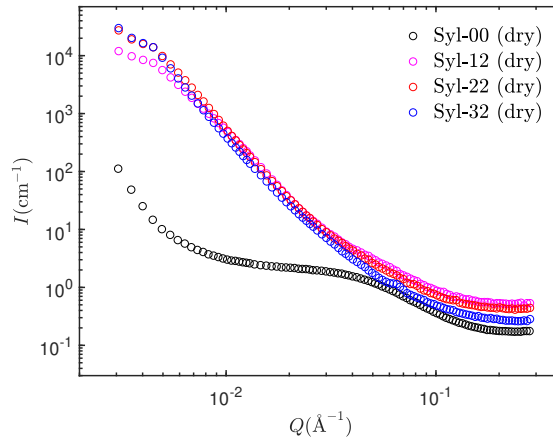


Figure S4: SAXS patterns of dry Syl IPNs.

setup	D (m)	C (m)	λ (Å)	Ap (mm ²)	t_{H_2O} (min)	t_{D_2O} (min)
1	19.505	20	19.60	49 × 49	30	30
2	19.505	20	10.31	49 × 49	20	10
3	7.605	8	5.15	50 × 50	10	5
4	1.605	4	5.15	45 × 45	5	5

Table S3

Experimental setups used in the SANS experiments. The given quantities are sample-detector distance (D), collimation length (C), neutron wavelength (λ), size of square source-side aperture (Ap), and measurement times used for samples soaked in H_2O (t_{H_2O}) and D_2O (t_{D_2O}). For all setups the sample-sided aperture was 6×6 mm² and the wavelength spread $\Delta\lambda/\lambda$ 10%.

0.48 \AA^{-1} . Setup 1 was not used for D_2O soaked samples due to poor overlap between it and the other setups, reasons for this are discussed below. Transmissions were measured with 20 m collimation and 7.605 m sample-detector distance for all samples at all three wavelengths used in the experiment. The samples were measured at room temperature ($\sim 25^\circ\text{C}$) in 1 mm path length sandwich cells, where the wet samples were placed with excess H_2O or D_2O between two 1.25 mm thick quartz windows.

For data reduction the *QtiKWS* software provided at the beamline was used. The two-dimensional raw data were corrected for background radiation and dark current (measured while blocking the beam with a boron carbide slab), transmission, sample thickness, detector sensitivity (measured with a 1.5 mm plexiglass sample) and the scattering of an empty sandwich cell. Measurements with the plexiglass standard were also used to put the data on an absolute scale. The thickness of the sandwich cells varied between 3.3 and 3.7 mm; a common sample thickness of 1 mm was used for all samples. (Different sample holders were used for these SANS measurements and the SESANS measurements in the main paper, and we were differently able to control the thickness in each.) The 2D patterns were azimuthally averaged to provide the scattered intensity (cm^{-1}) as a function of Q (\AA^{-1}). Since water scatters nearly flat in the small-angle scattering range, no subtraction of the water scattering was done. The scattering of the water and any other flat incoherent scattering is later considered by an additive constant in the fits.

S3.2. H_2O -swollen Sqr-IPN samples

A similar difference between scattering of D_2O and H_2O samples are seen for the whole sample series. The sample of Sqr with 34% hydrogel that is hydrated by H_2O and the sample of Sqr without hydrogel, on the other hand, look more similar, reflecting that soaking the samples in H_2O does not change the contrast very significantly. The increase in scattering at high- Q , can be identified as incoherent scattering from the ^1H nuclei of H_2O , and shows that the sample clearly has taken up water. The large increase in scattering when the hydrogel is filled with D_2O shows that highlighting the hydrogel is successful, and this indicates that the SANS data on the D_2O -hydrated sample series can be used to

investigate the hydrogel structure.

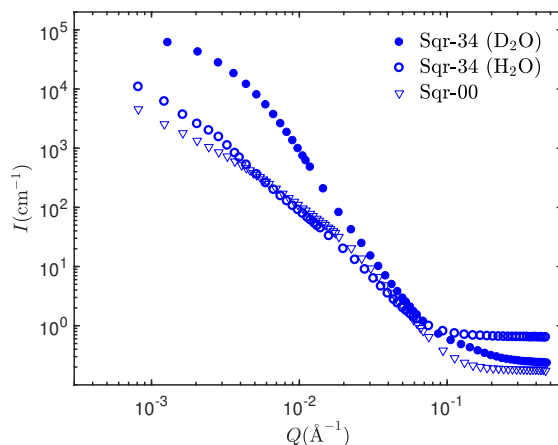


Figure S5: SANS data on Sqr-34 soaked in H₂O and D₂O and the pure and dry Sqr-00 sample. Not all data points are shown for clarity.

For the H₂O soaked samples, the contrast that the hydrogel, the silicone, and the silica have with the hydrating H₂O, as well as with each other, is much less than that between D₂O and all the other materials. This means that no one single species dominates the scattering, and therefore, complicates the data analysis, making it very complicated to fully model the data. The SANS data on the series of H₂O-hydrates Sqr-silicones is shown in Figure S6.

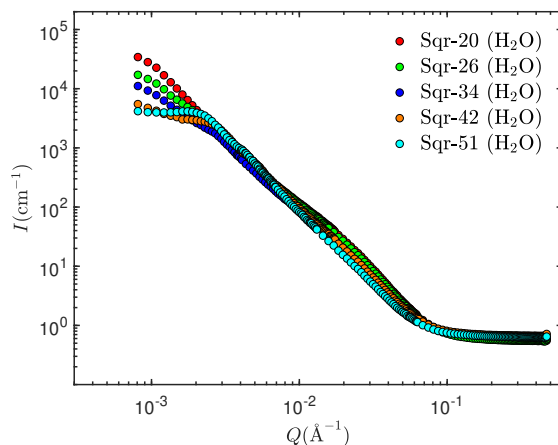


Figure S6: SANS data on the Sqr series samples soaked in H₂O.

The SANS data of the most dilute sample (Sqr-20 H₂O) can be successfully fit assuming the scattering intensity arises from the independent contributions: a flat background at high Q , the silica filler at intermediate Q (using the unified exponential power law model of Beaucage due to the unavailability of a mass-surface fractal model in SASfit), and spheres of hydrogel solvated with H₂O at low Q . The best fit dimensions of the spheres are a radius of 61 nm with a log-normal distribution width of 0.51.

S3.3. D₂O-swollen Sqr IPN samples

The SANS data (setups 2, 3, and 4) of the D₂O-hydrated IPNs measured at setups 2–4 could be merged together. However, the scale factor necessary for aligning the data obtained at different wavelengths (5.15 Å and 10.31 Å) was close to 2 which is worryingly high and indicates there could be a problem with multiple scattering in the 10.31 Å data. Merging the data obtained at 19.60 Å (setup 1) was not possible and the measured transmission was also

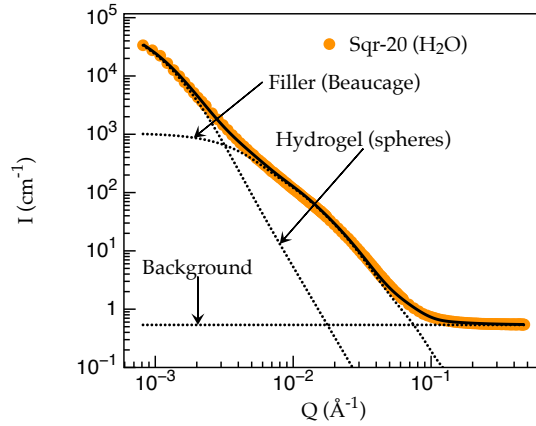


Figure S7: SANS data on the Sqr-20 sample soaked in H₂O fit to a three component model, with each shown in the figure.

very low, signifying that multiple scattering is clearly an issue at 19.60 Å. The data obtained at setup 1 was therefore discarded from the merged data shown in Figure S8. The scattering does not vary considerably with varying hydrogel concentration as can be seen. The same data were obtained for the Syl-22 sample, and the data were also qualitatively similar.

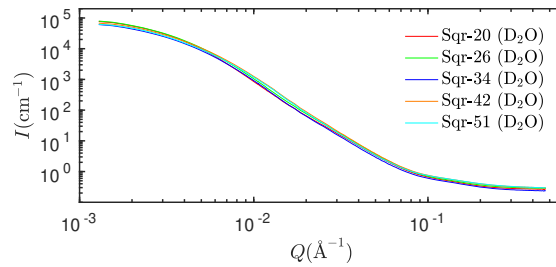


Figure S8: Merged SANS data on the D₂O-containing samples of the Sqr IPNs obtained using setups 2–4. The SANS curves show that the scattering from the different samples is very similar.

Due to very intense scattering, the individual detector configurations were modelled separately using a fitting routine that can account for multiple scattering, which has been implemented in the SASfit program. The multiple scattering intensity is calculated from the single scattering approximation, according to the literature.[? ?] The inputs for the calculation of multiple scattering effects are the neutron wavelength (in Å), the sample thickness (in cm), and the total scattering cross section per unit volume, Σ_t . The units of Σ_t must be the same units as the modulus of the momentum transfer vector Q (Å) and the sample thickness (cm), so for these measurements shown here, the units are Å⁻² cm⁻¹). Further details can be found in the latest version of the SASfit manual [?].

There are only a limited number of analytical models for calculating multiple scattering effects available. A model for spheres with a log-normal size distribution is available in SASfit [?], and this was used to fit the SANS data of the most dilute of the IPNs (Sqr-20) in its D₂O-swollen form using data from all four measurement setups.

In order to have reasonable and independent inputs for the multiple scattering fitting, we have refit the SESANS data for Sqr-20 (D₂O) using a sphere model with a log-normal distribution and no structure factor. We use the fit parameters from the sphere component alone (ignoring the long-range DAB contribution) for the multiple scattering calculation. The best fit values are a radius R of 71 nm, a log-normal width parameter σ of 0.58, and a total scattering cross-section Σ_t of 46.7 Å⁻² cm⁻¹. Considering that the size distributions are very broad, this compares favorably to the values fit using a structure factor (Robertus model for spheres with a Schulz distribution and a volume fraction ϕ fixed to 0.01), shown in Table 4 in the main paper. The best fit values using this model are a radius R of 95 nm, a Schulz width parameter σ of 0.76, and a total scattering cross-section Σ_t of 46.0 Å⁻² cm⁻¹. The fit to the SESANS

data using this dilute sphere model is shown in Figure S9.

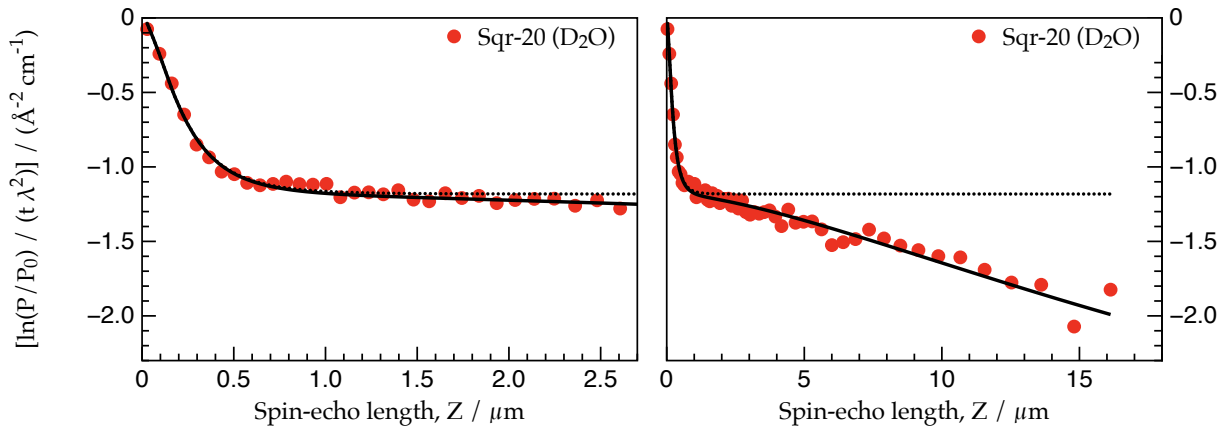


Figure S9: SESANS data of D₂O-hydrated Sqr-20. The solid lines show fits to both components (hydrogel spheres and long-range inhomogeneities), whereas the dotted lines show the contribution from the hydrogel spheres only. Left and right panels show data up to spin-echo lengths of 2.7 and 18 μm , respectively. This data in this plot are fit to a different sphere model (log-normal size distribution without a structure factor) than used in the main paper, to obtain inputs for the multiple scattering analysis.

The fit parameters for the spheres from the SESANS data modelling then became inputs for the multiple scattering analysis. Furthermore, two backgrounds are subtracted from the SANS data: a constant and a Beaucage model calculation for the filler (Figure S7). The multiple scattering analysis is then performed, fixing these parameters and varying the scale parameters for each of the SANS configurations and the two backgrounds.

To assess the impact of multiple scattering, the total amount of scattering was inputted using parameters using total scattering from the high Z plateau in the SESANS data and the radius and size distribution (dilute sphere model with a log normal size distribution) also from SESANS fitting. Values were inputted rather than fit to reduce the number of degrees of freedom. The results of this multiple scattering modeling for each instrument configuration are shown in Figure S10 (left). At high Q , the poor fit is due to background subtraction and low scattering intensity. At low Q , where the impact of multiple scattering is pronounced, there is good agreement between the data and the fit assuming multiple scattering, especially considering that only the scales and backgrounds are varied. Figure S10 also shows the calculated scattering, if the only contribution were single scattering, in the absence of multiple scattering. This difference shows why SANS with D₂O hydration is unable to determine the structure of the hydrogel, in general

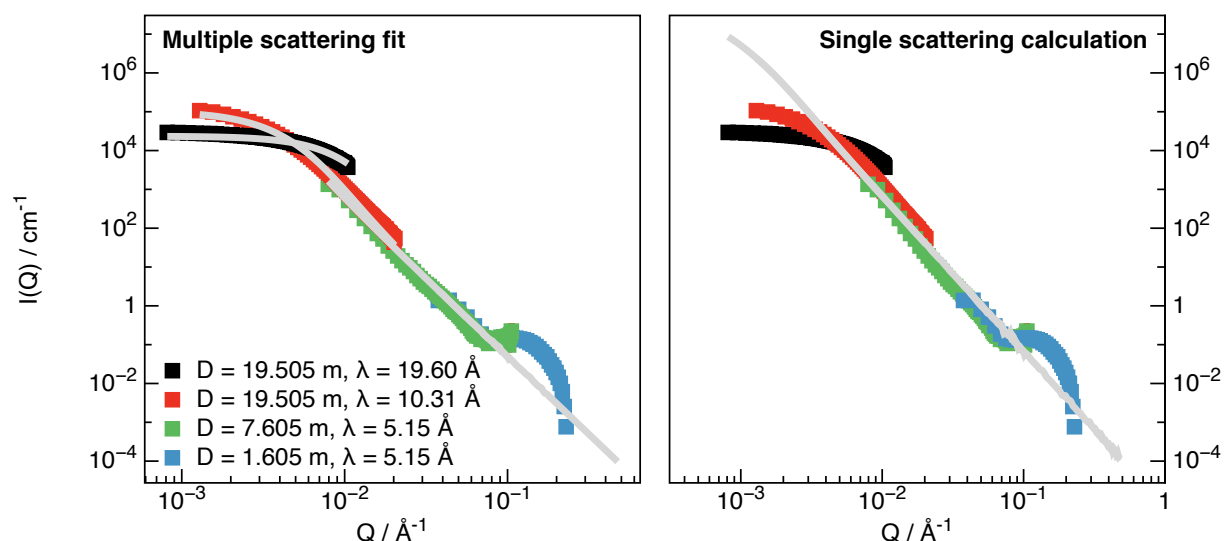


Figure S10: Multiple scattering analysis of SANS data of Sqr-20 (D_2O) at four instrument configurations, denoted in the legend. The parameters used are explained in the text. In general, there is very good agreement between the data and the scattering intensity calculated assuming multiple scattering (right). The calculated scattering for Sqr-20 (D_2O) in the absence of multiple scattering (right) shows significant differences below Q of 10^{-2} \AA^{-1} , where multiple scattering dominates.

References

- [] S. D. W., K. D. Keefer, D. W. Schaefer, K. D. Keefer, S. D. W., K. D. Keefer, Structure of Random Porous Materials: Silica Aerogel, *Phys. Rev. Lett.* 56 (1986) 2199–2202.
- [] A. J. Hurd, D. W. Schaefer, J. E. Martin, Surface and mass fractals in vapor-phase aggregates, *Phys. Rev. A* 35 (1987) 2361–2364.
- [] P. W. Schmidt, Small-Angle Scattering Studies of Disordered, Porous and Fractal Systems, *J. Appl. Cryst.* (1991) 414–435.
- [] A. Radulescu, V. Pipich, H. Frielinghaus, M. S. Appavou, KWS-2, the high intensity / wide Q-range small-angle neutron diffractometer for soft-matter and biology at FRM II, *J. Phys.: Conf. Ser.* 351 (2012) 012026.
- [] J. Schelten, W. Schmatz, Multiple-scattering treatment for small-angle scattering problems, *J. Appl. Cryst.* 13 (1980) 385–390.
- [] G. V. Jensen, J. G. Barker, Effects of multiple scattering encountered for various small-angle scattering model functions, *J. Appl. Cryst.* 51 (2018) 1455–1466.
- [] J. Kohlbrecher, User guide for the `sasfit` software package: A program for fitting elementary structural models to small angle scattering data (April 23, 2020), 2020. URL: <https://github.com/SASfit/SASfit/blob/master/doc/manual/sasfit.pdf>.